

# From large scale gas compression to cluster formation in the Antennae overlap region <sup>★</sup>

C. N. Herrera, F. Boulanger and N. P. H. Nesvadba

Institut d’Astrophysique Spatiale, UMR 8617 CNRS, Université Paris-Sud 11, 91405 Cedex Orsay, France

Preprint online version: October 13, 2011

## ABSTRACT

We present a detailed observational analysis of how merger-driven turbulence may regulate the star-formation efficiency during galaxy interactions and set the initial conditions for the formation of super star clusters. Using VLT/SINFONI, we obtained near-infrared imaging spectroscopy of a small region in the Antennae overlap region, coincident with the supergiant molecular cloud 2 (SGMC 2). We find extended H<sub>2</sub> line emission across much of the 600 pc field-of-view, traced at sub-arcsecond spatial resolution. The data also reveal a compact H<sub>2</sub> source with broad lines and a dynamical mass  $M_{\text{dyn}} \sim 10^7 M_{\odot}$ , which has no observable Brγ or K-band continuum emission, and no obvious counterpart in the 6 cm radio continuum. Line ratios indicate that the H<sub>2</sub> emission of both sources is powered by shocks, making these lines a quantitative tracer of the dissipation of turbulent kinetic energy. The turbulence appears to be driven by the large-scale gas dynamics, and not by feedback from star formation. We propose a scenario where the H<sub>2</sub> emission is related to the formation of bound clouds through accretion. The kinetic energy of the accreted gas drives the turbulence and powers the H<sub>2</sub> emission. Broad H<sub>2</sub> line widths of order 150 km s<sup>-1</sup>, similar to the velocity gradient of the gas across the field of view, support this idea. Within this interpretation, the compact H<sub>2</sub> source could be a massive cloud on its way to form a super star cluster within the next few Myr. This scenario can be further tested with ALMA observations.

**Key words.** Galaxies: interactions, ISM, starburst, star formation

## 1. Introduction

Detailed observations of the nearby Antennae galaxy merger NGC4038/4039 at a distance of only 22 Mpc (Schweizer et al. 2008) provide important benchmarks for our understanding of how the large-scale dynamics of galaxy interactions trigger star formation on much smaller scales. Contrary to the ‘canonical’ scenario of merger-induced star formation, which predicts intense starbursts in the nuclear regions (e.g., Barnes & Hernquist 1996), most stars in the Antennae are formed off-nucleus, in a heavily obscured, gas-rich, infrared-luminous region where both galaxies permeate each other, the “overlap region” (e.g., Vigroux et al. 1996; Klaas et al. 2010).

Most of the star formation in the overlap region of  $20 M_{\odot} \text{ yr}^{-1}$  (Zhang et al. 2001) occurs in massive super-star clusters (SSCs) with masses larger than  $10^4$  and up to a few  $10^6 M_{\odot}$  (Whitmore & Schweizer 1995; Zhang & Fall 1999; Whitmore et al. 2010). Detailed studies of SSCs constrain the recent star formation history of the overlap region. At typical ages of few  $10^6$  yrs, many SSCs have already expelled most of the gas and dust from their immediate surroundings, and they may be becoming unbound themselves (Fall et al. 2005; Mengel et al. 2005; Gilbert & Graham 2007; Fall et al. 2010).

Our understanding of how the galaxy interaction may trigger gas collapse and the very early phases in the formation of SSCs, is much less developed and relies mostly on theoretical arguments. For example, Scoville et al. (1986) suggested that the collision between the two galaxies could trigger collisions between pre-existing giant molecular clouds. Jog & Ostriker (1988) ar-

gueled that shock-heated ambient gas may enhance star formation by increasing the pressure in embedded molecular clouds. Keto et al. (2005) discuss their high resolution interferometric observations of molecular gas and the formation of massive star clusters in the starburst galaxy M82 within this scenario. However, observations of the Antennae overlap region may not be accounted for by the collapse of pre-shock clouds. The large surface density of molecular gas and its fragmentation in complexes with masses of several  $10^8 M_{\odot}$  (Wilson et al. 2000), two orders of magnitude larger than masses of giant molecular clouds in spiral galaxies, are evidence for cooling and gravitational fragmentation of the diffuse gas compressed in the galaxy collision.

First attempts to quantify the impact of the interaction on gas cooling and fragmentation have been made with numerical simulations (Teyssier et al. 2010; Karl et al. 2011, 2010), but their description of the energy dissipation of the post-shock, turbulent multiphase ISM is still schematic. The simulations follow the turbulent energy of the gas over a limited range of scales. The mechanical energy of the galaxy collision is thermalized in large-scale shocks and radiated away by the shock compressed post-shock gas. Observations of the galaxy-wide shock in Stephan’s Quintet (Appleton et al. 2006; Cluver et al. 2010) show that a dominant fraction of the collision energy is not thermalized in such shocks, but cascades to smaller scales into turbulent motion within molecular gas. This results from the clumpy multi-phase structure of the pre-shock interstellar medium (Guillard et al. 2009). The fact that most of the collision energy is transferred to the molecular gas has consequences for the energy dissipation and the gravitational fragmentation of the post-shock gas, and thereby for induced star formation, which have yet to be understood. It is the motivation of this paper to investigate how gas compression and turbulence driven by the

<sup>★</sup> Based on observations with the VLT/SINFONI, Program ID 383.B-0789, with the VLT/CRIRES, Program ID 386.B-0942, and with the CFHT/WIRCAM, Program ID 09AF98

large-scale dynamics of the two interacting galaxies trigger and regulate star formation in the Antennae overlap region.

Bright H<sub>2</sub> line emission powered by shocks (rather than star formation) has been identified in the diffuse interstellar medium of the Milky Way (Falgarone et al. 2005), as well as in a significant number of extragalactic systems including many interacting galaxies (Appleton et al. 2006; Cluver et al. 2010; Zakamska 2010). This makes emission-line observations of warm H<sub>2</sub> an interesting tracer of the dissipation of turbulent energy in the molecular gas. Haas et al. (2005) proposed, based on ISO observations, that H<sub>2</sub> line emission in the overlap region could probe large-scale shocks driven into molecular clouds. This was later called into question by Brandl et al. (2009), who found lower H<sub>2</sub> line fluxes with Spitzer-IRS, and suggested that the bulk of the warm molecular gas may be heated by star formation after all. However, at a spatial resolution of  $\sim 5''$ , and a spectral resolution of  $R = 600$  ( $\sim 500 \text{ km s}^{-1}$ ) Spitzer-IRS does not allow to study the molecular gas at the scales relevant for the fragmentation of the molecular gas,  $\leq 100 \text{ pc}$  and  $\sim 100 \text{ km s}^{-1}$ , respectively.

We use near-infrared spectroscopy obtained with the imaging spectrograph SINFONI and the echelle spectrograph CRIRES (both on the ESO Very Large Telescope) to quantify the dissipation of kinetic energy in the molecular gas on scales of few 10s to 100s of pc. To this end we observed the region around “knot 5” of Brandl et al. (2009), the brightest H<sub>2</sub> peak in the overlap region. This knot, which is near the massive and IR-bright cluster No. 28 of Whitmore et al. (2010), coincides with the super-giant molecular cloud SGMC 2 observed by Wilson et al. (2000) in CO. SGMC 2 is one of the most massive molecular clouds in the overlap region, with a mass of  $4 \times 10^8 M_{\odot}$ . Our pointing also coincides with knot K2a in the Herschel dust imaging of Klaas et al. (2010). Thus, overall, by selecting an area with particularly bright line emission of warm molecular hydrogen, we observed one of the main sites of molecular gas and star formation in the Antennae overlap region.

The paper is organized as follows. The observations and data reduction are described in Sect. 2. In Sect. 3 we focus on the structure and kinematics of the warm H<sub>2</sub> gas. We identify two components of H<sub>2</sub> emission: diffuse emission extended over the 600 pc wide field of view of SINFONI, and a compact source. We show that, for the compact and diffuse extended emission, the H<sub>2</sub> emission is powered by shocks rather than UV heating, and estimate the bolometric H<sub>2</sub> luminosity of each component combining Spitzer and SINFONI observations (Sect. 4). In Sect. 5 we propose an interpretation of the observations which relates the H<sub>2</sub> emission to the formation of bound clouds through gas accretion. In Sect. 6 we discuss the observations and our interpretation within a broader astrophysical context, highlighting the role of turbulence for the formation of super star clusters and the regulation of the star formation efficiency in galaxy mergers. Section 7 gathers the main conclusions.

## 2. Observations

### 2.1. VLT/SINFONI imaging spectroscopy

Our analysis is based on observations carried out with the near-infrared integral-field spectrograph SINFONI (Eisenhauer et al. 2003; Bonnet et al. 2004) on the ESO Very Large Telescope. Data were obtained in service mode under Program ID 383.B-0789 (PI Nesvadba). SINFONI is an image slicer with a field of view of  $8'' \times 8''$  and a pixel scale of 250 mas in the seeing-limited mode. The spectral resolution is  $R = 4000$  at  $\lambda = 2.2 \mu\text{m}$ . We observed three regions in the Antennae

galaxy merger in the  $K$ -band, one near each nucleus and one region in the overlap region. These pointings were selected based on their bright pure-rotational H<sub>2</sub> line emission detected with Spitzer/IRS. This paper presents an analysis of molecular emission of the pointing in the overlap region.

All data were taken in June and July 2009 under good and stable atmospheric conditions. We obtained a total of 1800 seconds of exposure time split into individual exposures of 600 seconds. We adopted a dither pattern where one sky frame was taken in-between two object frames to allow for an accurate subtraction of the night sky. Data reduction was done with the standard IRAF tools to reduce longslit spectroscopy (Tody 1993), which we extended with a set of SINFONI-specific IDL routines. For details see, e.g., Nesvadba et al. (2007, 2008). The telluric correction was done using bright ( $K \sim 6 - 8$  mag) stars observed at a similar air mass as our target. We used the light profiles of these stars to measure the PSF of our data,  $\text{FWHM} = 0''.7 \times 0''.6$ . Comparison with high-resolution HST/NICMOS imaging of Whitmore et al. (2010) shows that our PSF estimate is robust.

### 2.2. CRIRES high-resolution spectroscopy and CFHT narrow-band imaging

To complement our SINFONI observations we also obtained a high-resolution longslit spectrum with CRIRES on the VLT (program ID 386.B-0942; PI Herrera) and near-infrared imaging of the Antennae through the H<sub>2</sub> 1–0 S(1) and the Bry filters with WIRCAM at the Canada-France Hawaii Telescope (CFHT program ID 09AF98; PI Nesvadba).

With CRIRES we obtained a total of 5 hrs of integration time of the H<sub>2</sub> 1–0 S(1) line at  $2.12 \mu\text{m}$  in the rest-frame for one pointing centered on the compact molecular source (Sect. 3.3) and at position angle PA =  $67^\circ$ . Atmospheric conditions were good and stable. We nodded our target along the slit to ensure a robust sky subtraction. Data were dark-subtracted, flat-fielded, and sky subtracted. The wavelength calibration was done on telluric OH lines straddling the wavelength of the H<sub>2</sub> 1–0 S(1) line. Using a  $0.4''$  wide slit, we reached a spectral resolution of  $6 \text{ km s}^{-1}$ , a factor  $\sim 20$  higher than the effective resolution of our SINFONI data. This allowed us to analyze the line profile of the compact molecular source at a spectral resolution which is comparable to that reached by Wilson et al. (2000) for CO.

We determined the astrometry of the near-IR CFHT images through cross-correlation with the 2MASS  $K$ -band image of NGC4038/39. We give a short description of these data in Sect. 3.1. They have also been used to improve the astrometric accuracy of the SINFONI observations (Sect. 2.4).

### 2.3. Ancillary data sets

We complement our near-IR spectro-imaging data with CO(1–0) observations obtained with the Caltech Millimeter Array. C. Wilson generously shared her zeroth and first-moment maps of NGC4038/4039 with us. For a full discussion of these observations, see Wilson et al. (2000, 2003). Our SINFONI pointing in the overlap region coincides with their super-giant molecular cloud 2 (SGMC 2). Within the spatial resolution of the CO data, the peak of SGMC 2 coincides with the warm H<sub>2</sub> peak #5 in Brandl et al. (2009). In our analysis we adopt the mass, size and line width of SGMC 2 listed in Table 1 of Wilson et al. (2000).

In addition, we use published results from Spitzer/IRS mid-infrared spectroscopy by Brandl et al. (2009). Our pointing cor-

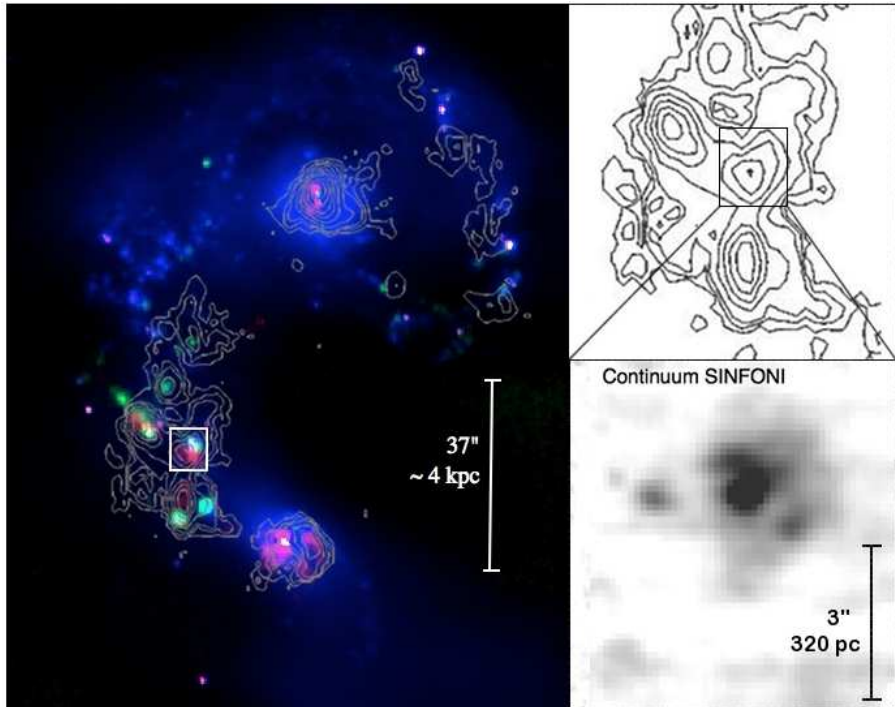


**Fig. 1.** Left panel: Central regions of the Antennae galaxy merger including both nuclei. The K-band continuum,  $\text{H}_2$  1–0 S(1), and  $\text{Bry}$  line emission are shown in blue, red, and green, respectively. All data were taken with WIRCAM on the CFHT. Grey contours show the CO(1–0) line emission from Wilson et al. (2000). The white square represents our SINFONI pointing. The  $\text{H}_2$  1–0 S(1) emission has the same morphology as the Spitzer IR emission in Brandl et al. (2009, their Fig. 4). The  $\text{H}_2$  morphology does not follow the continuum morphology, however, the  $\text{Bry}$  does. Right panel: Zoom onto the CO map of the overlap region (top, the square shows our SINFONI field of view) and the line-free K-band continuum morphology seen with SINFONI (bottom). North is up, and east to the left in all panels.

responds to their Peak #5. In Sect. 4.2 we will use the rotational  $\text{H}_2$  line fluxes from their Table 5 to compute the bolometric  $\text{H}_2$  luminosity. The integrated S(2) flux measured with the Short-High (SH) module is a factor 1.4 higher than that measured with the Short-Low (SL) module. Brandl et al. (2009) attribute this difference to the different apertures used for the SH and SL flux measurements. Since the aperture of the SH module ( $4''.4 \times 11''.3$ ) is best matched to the SINFONI field of view, we scale the S(3) flux, which was measured only with the SL module, by a factor 1.4.

#### 2.4. Astrometry of the SINFONI images

The SINFONI field-of-view is too small to register these data directly with astrometric catalogues. Therefore, to ensure that the absolute positional accuracy of our data is better than  $1''$ , we collapsed the SINFONI cube over the wavelength range of our CFHT  $K_s$ -band image, which we previously registered relative to the USNO catalog of astrometric standards, and matched the coordinates of both images. This gives a positional accuracy of  $\sim 0''.5$  for the SINFONI data. The position of the super-star cluster, the brightest continuum source in the SINFONI field of view, is within  $0''.5$  of archival HST/NICMOS images (taken through the F187N and F160W filters). Curiously, we find a  $2''$  offset relative to the coordinates of the super star cluster given by Whitmore et al. (2010, cluster #28 in their Table 8)

### 3. Observational results

In Sect. 3.1, we present the morphology and kinematics of the molecular and ionized gas. In the two following sections, we highlight the presence of extended  $\text{H}_2$  emission throughout the field (with broad  $\text{FWHM} \sim 150\text{--}200 \text{ km s}^{-1}$ , Sect. 3.2), and the discovery of a compact molecular source, with bright  $\text{H}_2$  line emission, which shows no  $\text{Bry}$ , nor continuum emission in the K-band (Sect. 3.3).

#### 3.1. Identification of individual components

The left panel of Fig. 1 shows the overall morphology of the continuum-subtracted  $\text{H}_2$  1–0 S(1) and  $\text{Bry}$  line emission in the Antennae.  $\text{H}_2$  emission is found in the two nuclei and in the overlap region.  $\text{Bry}$  is found in the overlap region with a different morphology than the molecular gas. Our SINFONI observations targeted the brightest peak in pure-rotational molecular line emission by Brandl et al. (2009). The field-of-view of our observations is marked by the white box. The right panel of Fig. 1 shows two zooms into this region.

In the SINFONI data cube we identify several emission lines from molecular ( $\text{H}_2$  1–0 S(0)→S(3),  $\text{H}_2$  2–1 S(1)), and ionized ( $\text{Bry}$ ,  $\text{He I}$ ) gas. Fig. 2 shows the maps of emission-line surface brightnesses, velocities, and FWHMs for  $\text{H}_2$  1–0 S(1) and  $\text{Bry}$ . A position-velocity diagram is shown in Fig. 1. Mean velocity and line widths were measured with Gaussian fits, carefully masking bad pixels. We also constructed a line-free continuum map (lower right panel of Fig. 1) by averaging the flux across the

**Table 1.** Parameters of the super star cluster in our field.

| Obs         | Size<br>''          | Age<br>Myr       | $A_K$<br>mag       | Mass<br>$\times 10^6 M_{\odot}$ | $N_{\text{ion}}$<br>$\times 10^{52} \text{ s}^{-1}$ | K<br>mag          | Reference               |
|-------------|---------------------|------------------|--------------------|---------------------------------|---|-------------------|-------------------------|
| HST         | —                   | 4.8 <sup>a</sup> | 0.8 <sup>a,b</sup> | 1.2 <sup>a</sup>                | —   | —                 | #28 from Table 8 in [1] |
| Keck + VLT  | 0''.46 <sup>c</sup> | 5.7 <sup>d</sup> | —                  | 4.1 <sup>e</sup>                | 1.3 <sup>e</sup>                                    | 15.2 <sup>f</sup> | SSC-C in [2]            |
| VLT/SINFONI | 0''.6 <sup>g</sup>  | < 6<br>4.5       | 0.4                | 6.0                             | 4.4 <sup>e,h</sup><br>6.6 <sup>i</sup>              | 15.0 <sup>f</sup> | Our work [3]            |

[1] Whitmore et al. (2010) based on ACS and NICMOS observations, [2] Gilbert & Graham (2007) based on Keck/NIRSPEC-SCAM and VLT/ISAAC observations, [3] For details see Sect. 3.1.

<sup>a</sup> from the comparison of integrated photometry UBV $I\text{H}\alpha$  with population synthesis models, <sup>b</sup> estimated from measured  $E(B - V) = 2.20$  and assuming  $R_V = 3.1$  extinction curve (Weingartner & Draine 2001), <sup>c</sup> deconvolved FWHM from Lorentzian fit, <sup>d</sup> based on the Bry equivalent width as an age indicator comparing it with Starburst99 (Leitherer et al. 2010) models, <sup>e</sup> not corrected for extinction, <sup>f</sup> K-band apparent magnitude for an aperture of 2'', <sup>g</sup> It is unresolved. The angular size (FWHM) measured from a Gaussian fit corresponds to the size of the seeing disk, <sup>h</sup> from observed Bry luminosity, <sup>i</sup> from the fluxes of the [Ne II] and [Ne III] lines at 12.81 and 15.56  $\mu\text{m}$ .

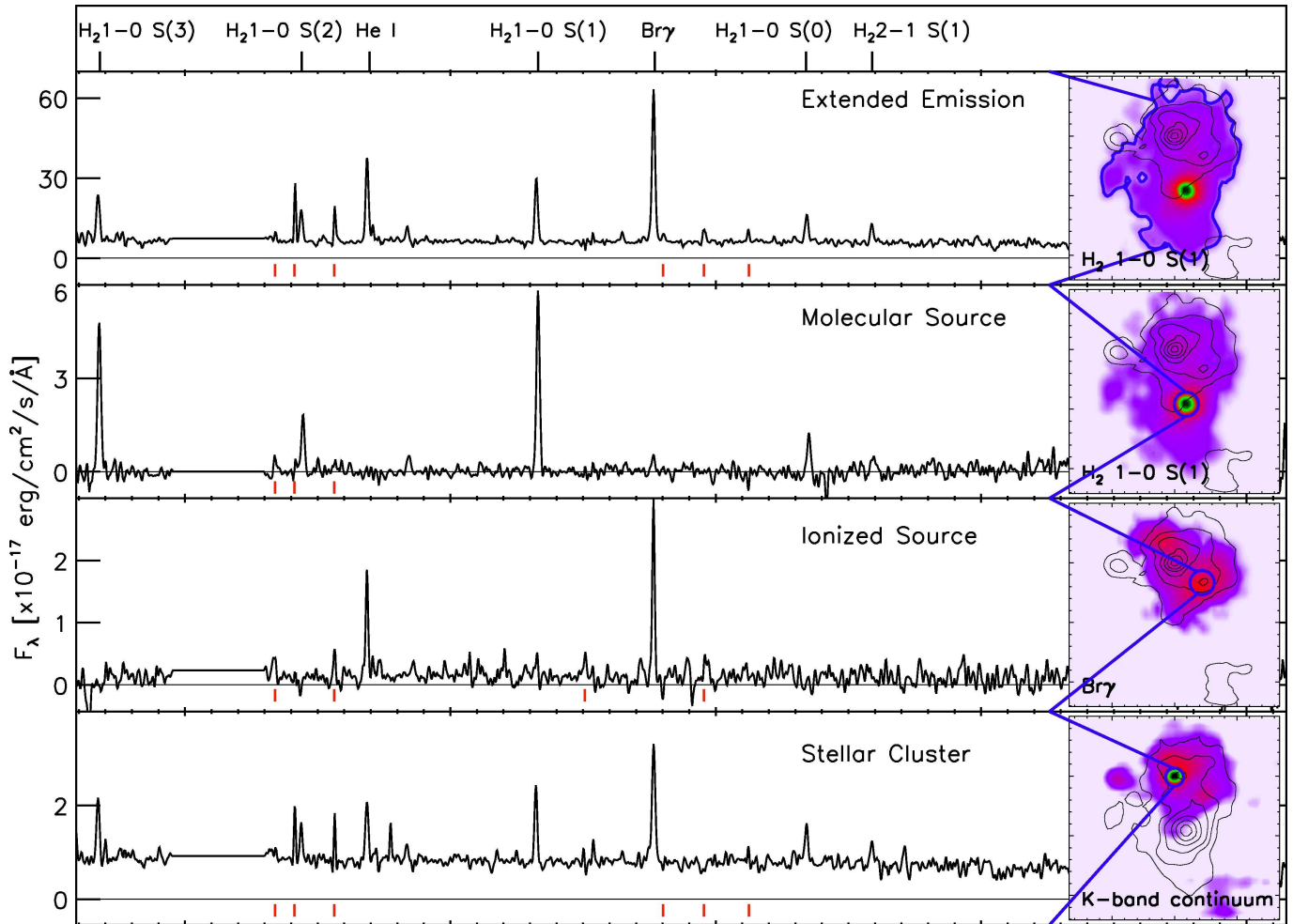


**Fig. 4.** Integrated SINFONI spectra for the four different components in our pointing of the overlap region of the Antennae. All spectra are smoothed by 3 bins in wavelength. Around 2.0  $\mu\text{m}$  the atmospheric transmission is very low so we did not plot this part of the spectra. We mark in red the wavelengths of the strong night sky lines seen in the spectra (OH lines). In the right panel, blue contours mark the aperture from which each spectrum was extracted.

full band in each spatial pixel after masking emission lines, bad pixels, and wavelengths affected by strong night-sky lines.

We identify 4 components in these maps: a compact continuum source (hereafter the super star cluster, SSC), two compact emission line sources (hereafter the molecular, and the ionized compact source, respectively) and diffuse extended emission.

The three compact sources are labelled in Fig. 4. The SSC has previously been identified with HST and Keck. The main parameters of the cluster are listed in Table 1. We estimated the stellar mass to  $6 \times 10^6 M_{\odot}$  from the K-band and Bry fluxes corrected for extinction (see Sect. 4.2.1), using Starburst99 (Leitherer et al. 1999), assuming solar metallicity, an instantaneous burst of age

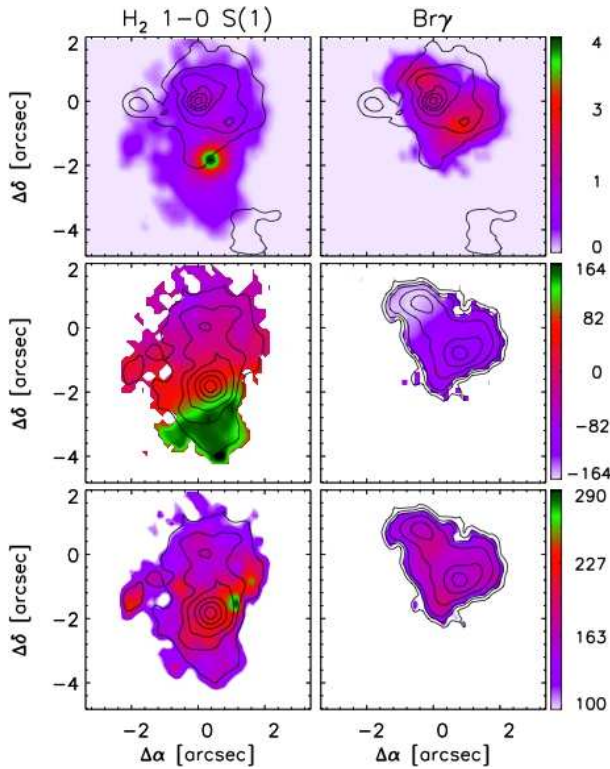


**Fig. 2.**  $\text{H}_2$  1–0 S(1) and Bry morphologies and kinematics. North is up, and East to the right in all panels. Top: Line surface brightnesses in units of  $\times 10^{-17}$  erg  $\text{s}^{-1}$   $\text{cm}^{-2}$ . The contours show the K-band continuum in steps of 15%, starting at 10% of the peak intensity,  $45 \times 10^{-20}$  erg  $\text{s}^{-1}$   $\text{cm}^{-2}$   $\text{\AA}^{-1}$ . Center: Velocities in  $\text{km s}^{-1}$  relative to the mean recession velocity in our field-of-view of  $1556 \text{ km s}^{-1}$ . Bottom: Measured FWHMs in  $\text{km s}^{-1}$ . All maps are spatially smoothed by averaging the original data over  $3 \text{ pixels} \times 3 \text{ pixels}$  ( $0.^{\circ}4 \times 0.^{\circ}4 \text{ pix}^{-1}$ ). The contours in the mid and lower images show the line surface brightness. Levels are 0.1, 0.2, 0.3, 0.5, 0.7, and 0.9 the peak intensity ( $3.8 \times 10^{-17}$  erg  $\text{s}^{-1}$   $\text{cm}^{-2}$  for  $\text{H}_2$  and  $2.6 \times 10^{-17}$  erg  $\text{s}^{-1}$   $\text{cm}^{-2}$  for Bry). Offsets are relative to the peak in the K-band continuum map,  $\alpha(J2000) : 12^{\circ}01'54\overset{''}{.}753$ ,  $\delta(J2000) : -18^{\circ}52'51\overset{''}{.}44$ .

4.5 Myr, and a Salpeter initial mass function with lower and upper mass cutoffs of 1 and  $100 M_{\odot}$ , respectively. Our upper age limit of 6 Myr is based on the absence of CO band-heads in the K-band spectrum and is consistent with previous measurements (Table 1). This cluster is one of the most massive clusters in the overlap region, and one of the brightest in the near-IR. The characteristics of the molecular and ionized compact sources are presented in Table 3.

The integrated spectra of each of the four components are presented in Fig. 4. In Table 2, we list line fluxes, mean velocities and line widths for the extended emission, and the molecular and ionized compact sources. To construct the spectrum of the extended emission, we integrated over the full spatial extent where  $\text{H}_2$  1–0 S(1) emission is observed, and subtracted the contribution from the compact sources. For the compact sources, we integrated within circular apertures of  $0.^{\circ}6$ ,  $0.^{\circ}8$ , and  $0.^{\circ}7$  (for the stellar cluster, the molecular and ionized sources, respectively) matched to their sizes. For the molecular and ionized sources we subtract the nearby background using an outer annulus. For the SSC, we do not see a distinct emission-line component that could be separated from the surrounding line emission.

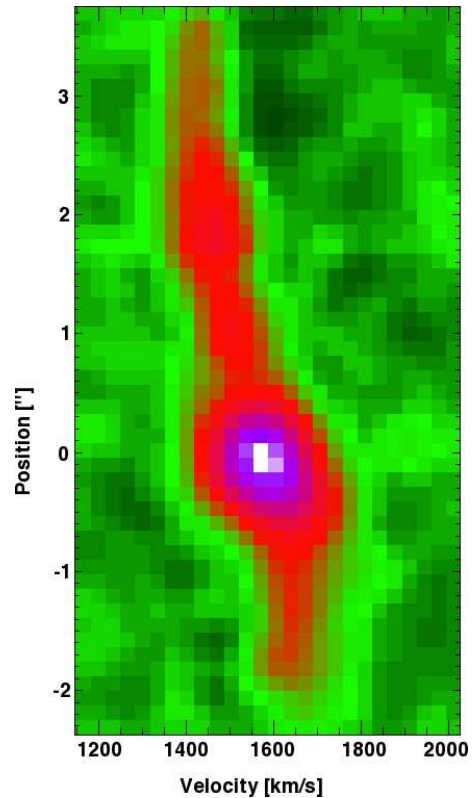


**Fig. 3.**  $\text{H}_2$  1–0 S(1) position - velocity diagram from north to south, at the position of the compact  $\text{H}_2$  source. The peak corresponds to the compact  $\text{H}_2$  source (Sect. 3.3). Positions are relative to this source.

Therefore, we did not subtract background line emission from the spectrum of the SSC. Had we done so, we would have obtained a pure continuum spectrum with no evidence of emission lines (not shown).

The spectra suggest that the astrophysical nature of these sources must be very different. For the extended line emission, we observe emission lines from both molecular and ionized gas. The molecular source shows only  $\text{H}_2$  lines and the ionized source only the Bry and  $\text{He I}$  emission lines. Fig. 5 presents a zoom onto the Bry and  $\text{H}_2$  1–0 S(1) lines for the extended emission-line region and the compact molecular source to illustrate the differences in line intensities and kinematics. For the extended emission, the velocities of the molecular and ionized gas are offset by  $\sim 100 \text{ km s}^{-1}$ . Throughout the rest of the paper we focus on the molecular emission, i. e., the  $\text{H}_2$  extended emission and the compact  $\text{H}_2$  source. The analysis of the ionized gas will be presented in a future publication.

### 3.2. Extended molecular emission

Fig. 2 shows extended  $\text{H}_2$  line emission over most of the field-of-view, with a morphology that is very different from that of Bry which is more concentrated around the SSC. The velocity field shows a systematic gradient of  $\sim 200 \text{ km s}^{-1}$  from northeast to south-west over a projected distance of 600 pc, giving an average velocity gradient of  $0.35 \text{ km s}^{-1} \text{ pc}^{-1}$ . Figure 3 shows the position - velocity diagram for the  $\text{H}_2$  1–0 S(1) line, along the direction of the velocity gradient (P.A.  $15^{\circ}$ ). The diagram is centered on the compact  $\text{H}_2$  source and reveals the velocity gradient and the high turbulence in the field. The  $\text{H}_2$  line widths of

$\text{FWHM} = 150 - 200 \text{ km s}^{-1}$  are comparable to the total gradient over the SINFONI field-of-view. The  $\text{H}_2$  line width is larger than those measured in Bry for the ionized gas (Fig. 5).

The  $\text{H}_2$  rotational lines observed with Spitzer (Brandl et al. 2009) are not spectrally resolved, the highest spectral resolving power of these data is  $R = 600$ , corresponding to  $\text{FWHM} = 500 \text{ km s}^{-1}$ . The CO(1–0) velocity ( $V_{\text{LSR}} = 1470 \text{ km s}^{-1}$ ) agrees with the mean, luminosity weighted, velocity of the  $\text{H}_2$  extended emission (Table 2). CO shows a velocity gradient as large as that of  $\text{H}_2$  but over larger distances. CO observations with a higher angular resolution are needed to resolve this gradient at the same scale as  $\text{H}_2$ . The warm  $\text{H}_2$  gas traced by the near-IR emission lines has line widths more than twice as large as those measured in CO at the same position ( $73 \text{ km s}^{-1}$  in Wilson et al. 2000).

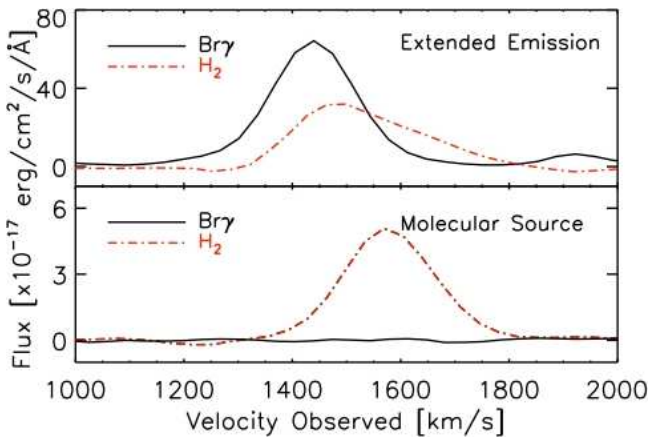


**Fig. 5.** Emission line profiles of molecular and ionized gas. Solid lines correspond to Bry and dot-dashed lines to  $\text{H}_2$  1–0 S(1). The kinematics of the extended molecular and ionized gas are different with an offset of  $\sim 100 \text{ km s}^{-1}$ . The molecular source shows broad  $\text{H}_2$  line emission and no Bry emission.

### 3.3. Compact molecular source

The  $\text{H}_2$  flux map in Fig. 2 reveals a compact source without a counterpart in the ionized gas and continuum emission. The spectrum of this source in Fig. 4 and 5 is unlike that of the other emission components. To our knowledge, this is the first time that an extragalactic source with a  $K$ -band spectrum showing only  $\text{H}_2$  lines is discovered. Similar spectra are seen in the Milky Way towards low-mass stars embedded in molecular clouds, which do not produce enough ionizing photons to power bright Hydrogen recombination lines (Giannini et al. 2006). In these sources the  $\text{H}_2$  emission traces shock heating of  $\text{H}_2$  associated with the interaction of the stellar jet with the molecular cloud.

Table 2 gives the  $\text{H}_2$  line fluxes and an upper limit on the Bry flux. The  $\text{H}_2$  1–0 S(1) flux of the molecular compact source accounts for 10% of the total emission from SGMC 2 in this line. To estimate the size of this source, we fit the azimuthally-averaged emission-line surface brightness profile along right ascension and declination with Gaussian curves. The FWHM size, geometrically averaged over the two axes, is  $0''.8$ . Correcting for the seeing we obtain an intrinsic source size of  $0''.5$  corresponding to 50 pc.

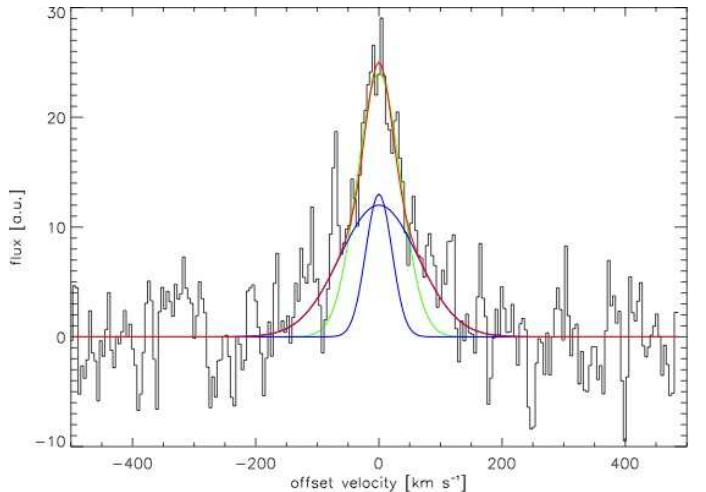


**Fig. 6.** Integrated spectra of the compact  $\text{H}_2$  source observed with CRIRES. Fitting the data with a single Gaussian (green line) shows significant residuals. An adequate fit (red line) requires 2 Gaussian curves (blue lines), corresponding to a narrow and a broad component, respectively.

We obtained high spectral resolution measurements of the line profile of the compact source with CRIRES (Fig. 6). Fitting this profile requires two Gaussian components with different line widths at a common velocity, with  $\text{FWHM}=50 \text{ km s}^{-1}$  and  $\text{FWHM}=160 \text{ km s}^{-1}$ , respectively. We illustrate this by showing fits with one and two Gaussians in Fig. 6. In the two-Gaussian fit, the narrow component contributes 25% to the total  $\text{H}_2$  line flux. We verified that we recover the line profile measured with SINFONI after convolution with the line spread function of SINFONI.

The compactness of the  $\text{H}_2$  source suggests that it is gravitationally bound, and that we can estimate the gas mass using the virial theorem. For a homogeneous spherical cloud the balance between gravitational and kinetic energy gives the virial mass as  $M_{\text{vir}} = 5 R \sigma^2/G$ , where  $R$  is the radius,  $\sigma$  the velocity dispersion of the gas, and  $G$  the gravitational constant. In this formula, we estimate the diameter using the FWHM size of the near-IR  $\text{H}_2$  emission. We obtain a virial mass of  $1.3 \times 10^7 \times (\sigma/21 \text{ km s}^{-1})^2 M_{\odot}$  using the line width of the narrow component detected with CRIRES for  $\sigma$ . The CO data do not have the required angular resolution to separate the compact source from the extended emission. High angular resolution observations with ALMA are required to estimate the virial mass from CO. The mass of the compact  $\text{H}_2$  source is a factor  $\sim 30$  smaller than the mass derived from CO observations for the SGMC 2 molecular complex (Wilson et al. 2000). From the virial mass and size, we derive the column density of the molecular source and we obtain  $N_{\text{H}} = 6 \times 10^{23} \text{ H cm}^{-2}$ . This corresponds to a mean density of  $6000 \text{ H cm}^{-3}$ .

Radio continuum maps at 6 cm show a slight excess ( $50 \mu\text{Jy}$ ) at the position of our molecular source (see Figures 5 and 9 in Neff & Ulvestad 2000). Assuming that this radio flux is entirely thermal emission from ionized gas, it corresponds to a Bry flux of  $\sim 5 \times 10^{-16} \text{ erg s}^{-1} \text{ cm}^{-2}$ . This value is a factor 5 larger than the upper limit on the observed Bry flux in Table 2 after scaling by our estimate of the extinction correction (a factor 20, see Table 3 and Sect. 4.2.1). This slight discrepancy could indicate that the newly formed stars are concentrated at the center of the cloud. In this case their emission could be more attenuated than the  $\text{H}_2$  emission. From the radio flux, we compute an ionizing photon

**Table 2.** Emission-line characteristics.

| Line                    | Rest Wavelength | Extended Emission |                       |                   | Molecular Compact Source |                       |        | Ionized Compact Source |                       |       |
|-------------------------|-----------------|-------------------|-----------------------|-------------------|--------------------------|-----------------------|--------|------------------------|-----------------------|-------|
|                         |                 | V <sub>LSR</sub>  | Flux×10 <sup>15</sup> | FWHM <sup>a</sup> | V <sub>LSR</sub>         | Flux×10 <sup>16</sup> | FWHM   | V <sub>LSR</sub>       | Flux×10 <sup>17</sup> | FWHM  |
| H <sub>2</sub> 1–0 S(3) | 1.95756         | 1490±17           | 6.1±0.4               | 225±14            | 1515±16                  | 6.5±0.2               | 167±7  |                        |                       |       |
| H <sub>2</sub> 1–0 S(2) | 2.03376         | 1461±18           | 3.3±0.3               | 234±18            | 1538±17                  | 2.3±0.1               | 140±11 |                        |                       |       |
| H <sub>2</sub> 1–0 S(1) | 2.12183         | 1493±17           | 6.9±0.3               | 215±9             | 1547±16                  | 7.6±0.1               | 146±2  | 1481±18                | 3.1±0.6               | <136  |
| H <sub>2</sub> 1–0 S(0) | 2.22329         | 1465±18           | 2.8±0.2               | 188±16            | 1554±18                  | 1.6±0.2               | 140±22 |                        |                       |       |
| H <sub>2</sub> 2–1 S(1) | 2.24772         | 1450±18           | 1.7±0.2               | 146±20            | 1530±26                  | 0.9±0.2               | 243±44 |                        | <0.36                 |       |
| Bry                     | 2.16612         | 1408±16           | 9.5±0.2               | 133±4             | 1443                     | <0.06                 |        | 1404±16                | 25.8±1.1              | 20±29 |
| He I                    | 2.05869         | 1410±16           | 5.2±0.2               | 131±7             |                          |                       |        | 1400±16                | 16.3±1.0              | 35±27 |
| Continuum <sup>b</sup>  |                 |                   | 0.06                  |                   |                          |                       |        |                        | 0.1                   |       |

Wavelengths are given in  $\mu\text{m}$ , fluxes in  $\text{erg s}^{-1} \text{cm}^{-2}$ , and velocities and FWHM in  $\text{km s}^{-1}$ . Error bars include the uncertainties in the wavelength calibration.

<sup>a</sup> intrinsic FWHM after deconvolution with the instrumental resolution of  $\sim 136 \text{ km s}^{-1}$ , <sup>b</sup> line-free  $K$ -band continuum flux in units of  $\text{erg s}^{-1} \text{cm}^{-2} \text{\AA}^{-1}$ .

rate of  $2 \times 10^{51} \text{s}^{-1}$ , which, for a young (1-2 Myr) burst corresponds to a stellar mass of  $\sim 4 \times 10^4 M_{\odot}$  based on Starburst99 models. This stellar mass is 0.3% of the virial mass of the compact H<sub>2</sub> source.

**Table 3.** Observed characteristics of the compact sources.

| Parameters                                | H <sub>2</sub> source               | H II source                       |
|---|-------------------------------------|-----------------------------------|
| Size                                      | 0'5                                 | 0'4                               |
| e <sub>c</sub>                            | ~20                                 | —                                 |
| n <sub>e</sub> [cm <sup>-3</sup> ]        | —                                   | 58 <sup>a</sup>                   |
| Mass [ $M_{\odot}$ ]                      | $1.3 \times 10^7$ <sup>b</sup>      | $4.8 \times 10^4$ <sup>c</sup>    |
| $N_{\text{ion}}$ [phot. s <sup>-1</sup> ] | $< 2.6 \times 10^{49}$ <sup>d</sup> | $8.5 \times 10^{50}$ <sup>e</sup> |
| $L_{\text{bol}}$ [ $L_{\odot}$ ]          | $2.6 \times 10^6$ <sup>f</sup>      | $5 \times 10^7$ <sup>g</sup>      |

<sup>a</sup> assuming ionization balance, and not correcting for extinction, scales as  $e_c^{0.5}$ .

<sup>b</sup> virial mass estimated from the intrinsic S(1) size and the CO line width.

<sup>c</sup> mass of the H II gas uncorrected for extinction, scales as  $e_c^{0.5}$ .

<sup>d</sup> from the upper limit of the Bry emission, uncorrected for extinction.

<sup>e</sup> derived from the Bry luminosity, scales as  $e_c$ .

<sup>f</sup> H<sub>2</sub> bolometric luminosity corrected for extinction (Sect. 3.3).

<sup>g</sup> from the age and  $N_{\text{ion}}$ . Uncorrected for extinction, scales as  $e_c$ .

## 4. The nature of the compact and diffuse H<sub>2</sub> emission

In this section we argue that, for both the extended emission and the compact molecular source, the H<sub>2</sub> line emission is shock powered. We also estimate the bolometric H<sub>2</sub> luminosity for both emission components.

### 4.1. Spectral diagnostics: PDR or shocked gas?

In this section, we discuss the excitation of the H<sub>2</sub> gas and the nature of the H<sub>2</sub> emission for the extended emission and the compact source. We focus on the near-IR lines within the  $K$ -band using spectral diagnostics that do not depend on extinction.

The H<sub>2</sub> excitation diagrams for the extended emission and the compact H<sub>2</sub> source are presented in Fig. 8. We obtain two

**Table 4.** H<sub>2</sub> line emission: Spectral diagnostics

| Component                     | H <sub>2</sub> 2–1/1–0 S(1) | H <sub>2</sub> 1–0 S(1)/Bry |
|-------------------------------|-----------------------------|-----------------------------|
| Extended emission             |                             |                             |
| Full area                     | 0.2                         | 0.72                        |
| Southern part                 | 3                           |                             |
| H <sub>2</sub> compact source | 0.1                         | >100                        |

estimates of the gas temperature, the first by fitting the H<sub>2</sub> population in the rotational states of the v=1 vibrational state, and the second from the ratio between the J=1 level of the v=1 and v=2 states. For the compact H<sub>2</sub> source we find 1700 K and 2300 K, respectively, and for the extended emission 900 K and 2700 K. The molecular gas has a range of temperatures. Most of the molecular gas is too cold to emit in the near-IR. The mass of warm gas seen in the near-IR is several orders of magnitude smaller than that observed in the mid-IR rotational lines by Brandl et al. (2009), and also much smaller than the virial mass given in Sect. 3.3. However, even though the mass is small, the energies are very large as we will see in Sect. 4.2.

The ratio  $R_{2-1/1-0} \equiv H_2 2-1 S(1)/H_2 1-0 S(1)$  is often used to discriminate between UV heating of H<sub>2</sub> in photodissociation regions (PDRs) and shock heating. The observed values of the extended emission and compact molecular source are 0.2 and 0.1, respectively. We compare these values with the Meudon PDR code described in Le Petit et al. (2006). Their Fig. 27 shows that PDRs typically have  $R_{2-1/1-0} = 0.5 - 0.6$ . Values of  $R_{2-1/1-0}$  in the range 0.1 to 0.2 are only reached for very high densities and strong radiation fields ( $n \gtrsim 10^5 \text{ cm}^{-3}$ ,  $\chi \gtrsim 10^5$ ). Such conditions do exist in massive star-forming regions, but only close to massive stars. This solution does not apply here because the compact H<sub>2</sub> source is far away from the SSC, and has no strong ionized line emission indicating the absence of massive young stars. For the compact source PDR emission is also ruled out by the ratio H<sub>2</sub> 1–0 S(0)/H<sub>2</sub> 1–0 S(1) (see Fig. 28 of Le Petit et al. 2006). The extended H<sub>2</sub> emission-line region extends over the whole field-of-view and does not peak at the position of the SSC. We therefore discard UV heating and favor shocks as main heating mechanism for the extended emission as well. Using the models of Kristensen (2007), we find that J-

and C-shocks match the observed values over a wide range of densities ( $10^4 - 10^6 \text{ cm}^{-3}$ ) and shock velocities ( $15 - 50 \text{ km s}^{-1}$ ).

The ratio  $R_{\text{S}(1)/\text{Bry}} \equiv \text{H}_2 \ 1-0 \ \text{S}(1)/\text{Bry}$  is an additional, more empirical diagnostics to identify the origin of the  $\text{H}_2$  excitation. These diagnostics provide additional evidence of shock excitation of  $\text{H}_2$  in our data. We compare our results for the Antennae overlap region with data presented by Puxley et al. (1990). Their data include 44 star-forming regions in 30 galaxies, where, typically, the  $\text{H}_2 \ 1-0 \ \text{S}(1)$  line is weaker than the Bry line (only 4 regions have a ratio higher than 1). Their flux ratios range between 0.1 and 1.5 with a mean of 0.5 and a dispersion of 0.3. A few sources such as the merger NGC 6240 show a much higher  $R_{\text{S}(1)/\text{Bry}}$  value. Puxley et al. (1990) present models for a number of different scenarios and conclude that the line emission is most likely from  $\text{HII}/\text{PDR}$  gas in massive star forming regions, for most of their sources. With our data, we obtain  $R_{\text{S}(1)/\text{Bry}} = 0.72$  and  $> 100$  for the extended emission and the compact source, respectively. The compact source shows a very high ratio, which is far from the typical range in star-forming galaxies. The ratio of the extended emission is within the range of observed and modeled values by Puxley et al. (1990). However, this is not true for all of the extended gas. In the region South of the bright Bry line emission (Fig. 7), we measure a ratio of 3. This value suggests that at least parts of the extended  $\text{H}_2$  emission is excited by shocks.

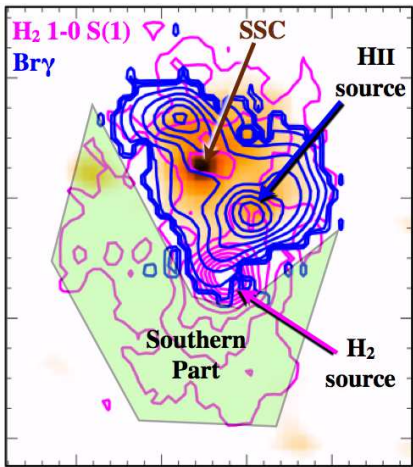


**Fig. 7.** The color image shows the  $K$ -band continuum, which peaks at the SSC. Pink and blue contours show the  $\text{H}_2 \ 1-0 \ \text{S}(1)$  and Bry emission, respectively. We also mark the compact ionized and molecular source (HII source and  $\text{H}_2$  source, respectively). The green area corresponds to the gas which is likely not influenced by the SSC, we call it 'Southern part'.

#### 4.2. $\text{H}_2$ bolometric luminosity

Before discussing the  $\text{H}_2$  emission as a coolant of the molecular gas in Sect. 5, we need to estimate the  $\text{H}_2$  bolometric luminosity of the extended emission and the compact source. This will be used in Sect. 5.2 and Sect. 5.3 to discuss what may power the  $\text{H}_2$  emission. To achieve this we combine the Spitzer and SINFONI  $\text{H}_2$  line measurements. This is not straightforward to do because the near-IR  $\text{H}_2$  is attenuated by dust extinction and the Spitzer angular resolution is too low to separate the contributions of the extended and compact source to the mid-IR rotational line emission. First, we estimate the near-IR extinction for

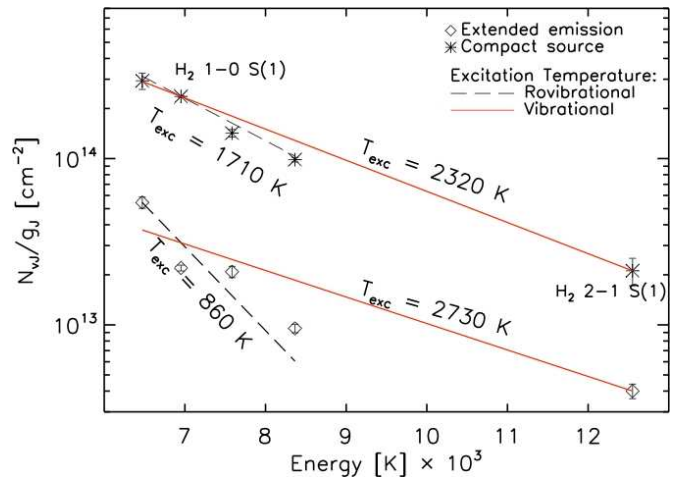


**Fig. 8.**  $\text{H}_2$  excitation diagram of the extended emission-line region and the compact source (Sect. 3.1). The dashed and solid red lines show the gas excitation temperature derived from fitting the  $\text{H}_2$  population in the rotational states of the  $v=1$  vibrational state, and from the ratio between the  $J=1$  level of the  $v=1$  and  $v=2$  states, respectively.

both emission components (Sect. 4.2.1). Second, we estimate the bolometric  $\text{H}_2$  luminosities, under the assumption that the fraction of the  $\text{H}_2$  luminosity in the  $\text{H}_2 \ 1-0 \ \text{S}(1)$  line is the same for the extended emission and the compact source (Sect. 4.2.2).

##### 4.2.1. Extinction correction

To quantify the extinction in the extended gas, we compare the number of ionizing photons  $N_{\text{ion}}$  obtained from the observed Bry emission line with that computed from the fluxes in the mid-IR  $[\text{Ne II}]12.8\mu\text{m}$  and  $[\text{Ne III}]15.6\mu\text{m}$  fluxes (Brandl et al. 2009). The extinction corresponds to the ratio between the two estimated values of  $N_{\text{ion}}$ . This ratio provides the effective extinction factor averaged over the entire field-of-view at the wavelength of Bry because the dust extinction of the mid-IR neon lines is much smaller than in the near-IR. The observed  $N_{\text{ion}}$  in the field-of-view was measured by integrating the Bry flux over the entire SINFONI cube. Assuming case B recombination, an electron density  $n_e = 10^2 \text{ cm}^{-3}$  and an electron temperature of  $T_e = 10^4 \text{ K}$  (see Table 8 of Hummer & Storey 1987),  $N_{\text{ion}} = 4.4 \times 10^{52} \text{ phot. s}^{-1}$ . To compute the  $N_{\text{ion}}$  from the Ne fluxes, we use the equations in Ho & Keto (2007) and the  $[\text{Ne II}]12.8\mu\text{m}$  and  $[\text{Ne III}]15.6\mu\text{m}$  fluxes. We further assume that  $n_e$  is smaller than the critical density,  $\sim 10^5 \text{ cm}^{-3}$ , and adopt the galactic Neon abundance. We obtain  $N_{\text{ion}} = 6.6 \times 10^{52} \text{ phot. s}^{-1}$ . Comparing with the result for Bry this suggests an extinction factor of 1.5.

The compact source has a very high column density,  $N_H = 6 \times 10^{23} \text{ H cm}^{-2}$  (Sect. 3.3), and therefore, the extinction must be much higher. Using the Milky Way extinction curve for  $R_V = 3.1$  in Weingartner & Draine (2001) this column density corresponds to  $\tau_{\text{ext}} = 30$  in the  $K$ -band. We roughly estimate the extinction correction from  $\tau_{\text{ext}}(K)$  with a simple toy model. We compute the attenuation due to the dust absorption for every point of a spherical and homogeneous cloud of constant density and line emission per unit volume. The flux that reaches the surface of the cloud depends on the path length  $l$ , and is attenuated by a factor  $e^{-\tau_{\lambda}(l)}$ . The optical depth  $\tau_{\lambda}(l) = \kappa_{\lambda} \rho \times l$  depends on the absorption coefficient at a given wavelength  $\kappa_{\lambda}$  and the

mass density  $\rho$ . The  $\kappa_\lambda$  value is taken from the  $R_V = 3.1$  curve in Weingartner & Draine (2001). We sum the attenuated emission over the cloud and compare the result with the total emission for zero opacity. We find a correction factor  $e_c = 0.7 \times \tau_{\text{ext}}$ . We also run the model with a density and emission profile  $\rho \propto r^{-2}$  for which we find  $e_c = 0.6 \times \tau_{\text{ext}}$ . In the following we only apply this extinction correction ( $e_c = 20$ ) to the narrow component of the H<sub>2</sub> line emission. In our interpretation of the data, the broad component is likely to come from the surface of the cloud, for which the extinction correction should be about a factor of 2, because we do not see the emission behind the cloud.

#### 4.2.2. Bolometric correction

The angular resolution of Spitzer/IRS is only 5'', too low to measure the total H<sub>2</sub> luminosity,  $H_2^{\text{bol}}$ , including the pure-rotational mid-IR lines, of the compact source directly. To circumvent this difficulty, we need to make an assumption. We assume that the  $H_2^{\text{bol}} / H_2$  1–0 S(1) ratio, after extinction correction, is the same for the compact source and for the extended emission. The detailed shock modelling which would be needed to support or refine this assumption is beyond the scope of this observational paper. The total H<sub>2</sub> luminosity (extended and compact source) is taken from the observations by Brandl et al. (2009), assuming that most of the H<sub>2</sub> emission is from the first four rotational lines. Within these simplifying assumptions, we find bolometric H<sub>2</sub> luminosities of  $L_{H_2} = 5.4 \times 10^6$  and  $2.6 \times 10^6 L_\odot$  for the extended and compact emission, respectively.

The extinction correction introduces significant uncertainties to these luminosities, in particular for the compact source. The total H<sub>2</sub> luminosity (extended emission + compact source) does not depend on extinction because most of the H<sub>2</sub> emission is from the mid-IR v=0 rotational lines measured by Spitzer for which extinction is negligible. It is the ratio between both luminosities which depends on the extinction correction. We set a lower limit of  $8 \times 10^5 L_\odot$  on the luminosity of the compact source by assuming that the extinction is the same for both components. The H<sub>2</sub> 1–0 S(1) emission represents 3% of the bolometric H<sub>2</sub> emission.

## 5. From large scale gas compression to star formation

The results presented in the previous sections raise three questions. How were the extended molecular gas component and the compact H<sub>2</sub> source formed? Why is this gas so H<sub>2</sub> luminous? What is the nature of the compact H<sub>2</sub> source? In this section, we argue that the extended emission traces highly turbulent molecular gas formed where the galaxy interaction is driving a large scale convergent flow. We relate the H<sub>2</sub> emission to the dissipation of the gas turbulent kinetic energy and the formation of the SGMC 2 complex and the compact H<sub>2</sub> source by gas accretion (Sect. 5.2). In Sect. 5.3 we argue that the compact H<sub>2</sub> source is a massive core on its way to forming a super star cluster.

### 5.1. Gas compression and gravitational fragmentation

The Antennae merger is close to pericenter passage when tidal forces are compressive (Renaud et al. 2008, 2009). Thus, we consider that the velocity gradient observed with the H<sub>2</sub> line emission across the SINFONI field is tracing a convergent flow driven by the galaxy interaction. The associated gas compression has created the conditions for the gas to cool and to be-

come molecular, like in numerical simulations of convergent flows (Hennebelle et al. 2008). As observed in the galaxy collision in Stefan's Quintet, the mechanical energy of the interaction is not fully thermalized in large scale shocks (Guillard et al. 2009). Due to the inhomogeneous, multi-phase, nature of the interstellar medium much of the gas kinetic energy decays from large to small scales before it is dissipated. Thus, we consider that it is the galaxy interaction that drives the molecular gas turbulence. This interpretation is supported by the fact that the large velocity gradient has the same magnitude as the turbulent line width, and by numerical simulations, which illustrate how dynamical and thermal instabilities lead to the formation of highly structured and turbulent molecular clouds where gas flows collide (Heitsch et al. 2005; Vázquez-Semadeni et al. 2007; Hennebelle et al. 2008).

The gas surface density is high enough for the turbulent gas to gravitationally contract and fragment within the time scale over which the tidal forces are compressive ( $\sim 10$  Myr, Renaud et al. 2008). We compute the Jeans length ( $R_{\text{Jeans}} = 5\sigma^2/(2\pi G\sigma)$ ) and mass ( $M_{\text{Jeans}} = \pi R_{\text{Jeans}}^2 \sigma$ ) using the CO(1–0) observations of Wilson et al. (2000) to estimate the gas velocity dispersion ( $\sigma$ ) and surface density ( $\sigma$ ). The value of  $\sigma$  is 30 km s<sup>-1</sup>. The surface density  $\sigma$  is obtained taking the ratio between the total virial mass and the total area of the overlap region  $\sigma \sim 500 M_\odot \text{ pc}^{-2}$ . We find  $R_{\text{Jeans}} \approx 350 \text{ pc}$  and  $M_{\text{Jeans}} = 2 \times 10^8 M_\odot$ . To compute the free-fall time scale  $\tau_{\text{ff}} = \sqrt{3\pi/(32\rho G)}$  we determine the mean density  $\rho$  from  $R_{\text{Jeans}}$  and  $M_{\text{Jeans}}$ . We find  $\tau_{\text{ff}} = 8 \text{ Myr}$ .

The Jeans length and mass are comparable to the size of the super giant molecular complex SGMC 2. It is thus likely that the complex has formed by gravitational contraction out of the gas compressed by the galaxy interaction. The gravitational contraction could contribute to the H<sub>2</sub> velocity gradient. An estimate of the motions driven by the self gravity of the complex is obtained taking the ratio between the free-fall velocity  $v_{\text{ff}} = 2 R_{\text{Jeans}}/\tau_{\text{ff}} \approx 90 \text{ km s}^{-1}$  and the Jeans radius. We find a value comparable to the velocity gradient measured with the H<sub>2</sub> line emission (200 km s<sup>-1</sup> over 600 pc). This calculation provides an upper limit to the velocity gradient from the cloud contraction since it is unlikely that the complex is free-falling. The cloud contraction must occur at a slower rate than free-fall because it takes time to dissipate turbulent energy (Elmegreen 2007; Huff & Stahler 2007).

Thus, we propose that the SGMC 2 complex is formed by convergent gas flows driven by the galaxy interaction and the gas self-gravity. Wilson et al. (2000) find that the gas mass inferred from the CO line luminosity matches the virial mass estimated from the CO line width and conclude that the SGMC 2 complex is gravitationally bound. In the remainder of this paper we use 'CO complex' to refer to gravitationally bound gas in the SGMC 2 complex. The velocity gradient and line width of the H<sub>2</sub> emission are both larger than the CO line width, suggesting that not all gas in the SGMC 2 complex is gravitationally bound. Most of the H<sub>2</sub> emission arises from gas that is unbound.

In the next two sub-sections we will interpret our H<sub>2</sub> data within this scenario. We associate the H<sub>2</sub> emission with the formation of the CO complex through gas accretion. We argue that the H<sub>2</sub> emission traces the dissipation of kinetic energy, which is required for gas that is driven by the galaxy interaction to become gravitationally bound.

## 5.2. The energetics and formation of the SGMC 2 complex

From observations of the Milky Way (Falgarone et al. 2005), and, more recently, of extragalactic sources (Guillard et al. 2009; Nesvadba et al. 2010; Ogle et al. 2010), we know that H<sub>2</sub> line emission is a major coolant of the ISM associated with the dissipation of interstellar turbulence. The H<sub>2</sub> line emission may arise from shocks, as quantified by models such as Flower & Pineau Des Forets (2010), and from friction between ions and neutral species in vortices (Godard et al. 2010). Models show that other emission lines contribute to the gas cooling but that they do not change the order of magnitude of the cooling rate (Flower & Pineau Des Forets 2010; Godard et al. 2010). Based on this earlier work, we consider the extended H<sub>2</sub> emission from SGMC 2 as a quantitative tracer of the dissipation rate of the kinetic energy of the gas.

Since the H<sub>2</sub> line widths and the velocity gradient across SGMC 2 is twice the CO line width, the H<sub>2</sub> emission does not come solely from the dissipation of the turbulent kinetic energy of the CO complex. A significant fraction of the emission must come from the dissipation of bulk and turbulent kinetic energy of gas driven by the galaxy interaction. Such a loss of kinetic energy is a required step for this gas to become gravitationally bound.

In the following, we quantify this interpretation which connects the energetics of the H<sub>2</sub> gas to the formation of the CO complex by gas accretion. We consider that the CO complex evolves in a quasi-static way assuming that virial equilibrium applies at all times. The virial equation relates the gravitational and turbulent kinetic energy,  $E_{\text{grav}}$  and  $E_{\text{turb}}$ , and includes the external pressure  $P_{\text{ext}}$ :

$$E_{\text{grav}} + 2 E_{\text{turb}} = 3 P_{\text{ext}} V \quad (1)$$

where  $V$  is the volume. The turbulent energy is  $E_{\text{turb}} = 3/2 M_{\text{CO}} \sigma_{\text{CO}}^2$ , where  $M_{\text{CO}}$  is the mass of the CO complex and  $\sigma_{\text{CO}}$  is the velocity dispersion along the line of sight derived from the integrated CO spectrum of SGMC 2. For a fixed  $P_{\text{ext}}$ , the exchange of energy associated with gas accretion and radiation is associated with the derivative of the enthalpy  $H$  of the complex (Huff & Stahler 2007):

$$\dot{H} = \dot{E}_{\text{grav}} + \dot{E}_{\text{turb}} + P_{\text{ext}} \dot{V} = -\dot{E}_{\text{turb}} + 4 P_{\text{ext}} \dot{V} = \dot{E}_{\text{in}} - L_{\text{H}_2}/f_{\text{H}_2} \quad (2)$$

where  $\dot{E}_{\text{in}}$  is the energy input from gas accretion,  $L_{\text{H}_2}$  the H<sub>2</sub> luminosity, and  $f_{\text{H}_2}$  the fraction of the gas bolometric luminosity that is radiated in the H<sub>2</sub> lines used to compute  $L_{\text{H}_2}$ . This fraction is smaller than 1 because some cooling occurs in lines which have not been measured. Combining H<sub>2</sub> and far-IR observations, Maret et al. (2009) find that  $f_{\text{H}_2}$  is in the range  $\sim 0.25 - 0.5$  for shocks associated with gas outflow from low mass stars. We assume that the kinetic energy of the accreted gas is the main source of energy that balances radiative losses (Klessen & Hennebelle 2010). In doing this we neglect the energy that comes from stellar feedback. The fact that the H<sub>2</sub> emission shows no enhancement around the SSC is an indication that stellar feedback does not have a significant contribution to the H<sub>2</sub> emission (Sect. 6.4).

We follow Klessen & Hennebelle (2010) in introducing the efficiency factor  $\epsilon$  which represents the fraction of the accretion energy that drives turbulence. The turbulent energy dissipates over a time scale  $t_{\text{dis}}(\text{CO}) \simeq R/\sigma_{\text{CO}}$  where  $R \simeq 300$  pc is the radius of the SGMC 2 complex (McKee & Ostriker 2007). The balance equation between energy input and dissipation is:

$$\epsilon \times \dot{E}_{\text{in}} = 3/2 M_{\text{CO}} \times \sigma_{\text{CO}}^3 / R \quad (3)$$

We compute the mass accretion rate necessary to drive the gas turbulence by equating the energy input and the radiative losses. This corresponds to a solution of equation (2) where the derivative of the gas kinetic energy  $\dot{E}_{\text{turb}}$  and the term associated with  $\dot{V}$  are both small with respect to the right-hand terms. Thus, we write:

$$\dot{E}_{\text{in}} = 3/2 \dot{M}_{\text{acc}} \sigma_{\text{H}_2}^2 \simeq L_{\text{H}_2} / f_{\text{H}_2} \quad (4)$$

where  $\sigma_{\text{H}_2}$  is the velocity dispersion along the line of sight derived from the H<sub>2</sub> data. To quantify  $\dot{M}_{\text{acc}}$  and  $\epsilon$ , we consider only the turbulent component of the velocity field ( $\text{FWHM}_{\text{H}_2} \sim 150$  km s<sup>-1</sup>), assuming that accretion occurs from turbulent gas with a mean velocity equal to that of the CO complex. For  $\sigma_{\text{H}_2} = 65$  km s<sup>-1</sup> and  $\sigma_{\text{CO}} = 30$  km s<sup>-1</sup>, we find  $\dot{M}_{\text{acc}} = 5.3/f_{\text{H}_2} M_{\odot} \text{ yr}^{-1}$  and  $\epsilon = 1.8 \times f_{\text{H}_2}$ . For our interpretation to hold we must have  $\epsilon < 1$ , and thus  $f_{\text{H}_2} < 0.5$ . The fact that the H<sub>2</sub> line width is larger than that of CO shows that this holds. In the following, for numerical calculations, we consider that  $f_{\text{H}_2} \sim 0.25$ .

We scale  $\dot{M}_{\text{acc}}$  by the turbulence dissipation time scale to estimate the mass of gas from which accretion is occurring:  $M_{\text{acc}} = \dot{M}_{\text{acc}} \times t_{\text{dis}}(\text{H}_2)$ , where  $t_{\text{dis}}(\text{H}_2) \simeq R/\sigma_{\text{H}_2}$  is the turbulent dissipation time scale. The large scale flow can feed this mass reservoir, compensating for what is accreted by the CO complex, because the dissipation time scale is comparable to the dynamical time scale associated with the velocity gradient across SGMC 2 ( $3 \times 10^6$  yr). We find  $M_{\text{acc}} = 2.4 \times 10^7/f_{\text{H}_2} M_{\odot}$ . For  $f_{\text{H}_2} \sim 0.25$ ,  $M_{\text{acc}}$  is 25% of  $M_{\text{CO}}$ . Thus, the mean density in the CO complex may only be a few times larger than that of the accreted gas. This agrees with our estimate of the efficiency factor  $\epsilon$ . Based on their numerical simulations and theoretical arguments, Klessen & Hennebelle (2010) argue that the efficiency factor  $\epsilon$  is roughly equal to the ratio between the density of the accreting gas to the mean density of the bound system.

Computing the ratio between the CO mass of SGMC 2 and the mass accretion rate, we obtain a time scale  $t_{\text{acc}} = 7 \times 10^7 \times f_{\text{H}_2}$  yr. For  $f_{\text{H}_2} \sim 0.25$ , this is slightly longer than the 10 Myr time scale over which the dynamics of the interaction may have been driving the convergent flow (Renaud et al. 2008). However, within the uncertainties in this rough calculation, we consider that the present accretion rate is close to the mean rate needed to account for the formation of the SGMC 2 complex as a result of gravitational fragmentation and gas accretion driven by the galaxy interaction.

Our interpretation introduces a dynamical view of the present state of the SGMC 2 complex. The virialized CO complex is physically associated with gas which is too turbulent to be bound. This unbound gas is dynamically fed by the convergent flow. It contributes an accretion flow onto the CO complex, which has the necessary magnitude to drive the gas turbulence, i.e. to balance the dissipation of the gas turbulent kinetic energy. Klessen & Hennebelle (2010) have proposed a similar interpretation to account for the formation and subsequent growth of turbulent molecular clouds in the LMC. In Sect. 6.3, we discuss the impact of this interpretation on the star formation efficiency within SGMC 2.

## 5.3. The nature of the compact H<sub>2</sub> source

In this section we extend our interpretation of the extended H<sub>2</sub> emission to the compact H<sub>2</sub> source. Like for the SGMC 2 complex we propose an interpretation where the H<sub>2</sub> luminosity traces the dissipation of the turbulent energy of the gas and gas accretion.

As a first test whether this is a plausible interpretation, we compare the dissipation rate of the turbulent energy of the gas with the H<sub>2</sub> luminosity of the source. Combining equations (3) and (4), we obtain an equation that we can use to estimate the mass of the compact source,  $M_{\text{cloud}}$ , from the H<sub>2</sub> luminosity.

$$3/2 M_{\text{cloud}} \times \sigma_v^3 / R = \epsilon \times L_{\text{H}_2} / f_{\text{H}_2} \quad (5)$$

where  $\sigma_v = 20 \text{ km s}^{-1}$  based on the width of the narrow component in the CRIRES spectrum (FWHM = 50 km s<sup>-1</sup>). We find

$$M_{\text{cloud}} = 2.7 \times 10^7 \times \epsilon / f_{\text{H}_2} \times (L_{\text{H}_2} / 2.6 \times 10^6 L_\odot) M_\odot \quad (6)$$

This mass estimate depends on the ratio  $\epsilon / f_{\text{H}_2}$ . Assuming that this ratio is  $\sim 1$  as estimated for the CO complex, we find a mass slightly larger than the virial mass  $M_{\text{vir}} = 1.3 \times 10^7 M_\odot$  derived for the same velocity dispersion in Sect. 3.3. We conclude from this comparison that the H<sub>2</sub> emission from the compact source may be accounted for by the dissipation of turbulent kinetic energy if the source is a gravitationally bound cloud with a mass in the range 1 to a few  $10^7 M_\odot$ . With this interpretation, the compact H<sub>2</sub> source is a gravitationally bound cloud, massive enough to form a super star cluster.

Like what we have done in the previous section for the CO complex, we can use equation (4) to estimate the mass accretion rate and thereby the cloud formation time scale. For  $\sigma_{\text{H}_2}$ , we use the width of the broad component (FWHM = 160 km s<sup>-1</sup>) in the line profile of the 1–0 H<sub>2</sub> S(1) measured with CRIRES. We find:

$$\dot{M}_{\text{acc}} = 9.2 \times \left( \frac{f_{\text{H}_2}}{0.25} \right)^{-1} \times \left( \frac{L_{\text{H}_2}}{2.6 \times 10^6 L_\odot} \right) M_\odot \text{ yr}^{-1} \quad (7)$$

The ratio between  $M_{\text{cloud}}$  and  $\dot{M}_{\text{acc}}$  yields a cloud formation time scale by accretion of  $t_{\text{acc}} = 2.9 \times 10^6 \times (\epsilon / 0.25) \text{ yr}$ . This value is about twice the cloud dynamical time  $R / \sigma_v$ . We would thus be observing a pre-cluster cloud early in its evolution. Even at this early stage it is remarkable that the fraction of the cloud mass that has been transformed into stars is very small ( $\sim 0.3\%$ , Sect. 3.3). We observe that the cloud has formed and become gravitationally bound without having formed massive stars.

If our interpretation is correct, by observing the gas cooling through H<sub>2</sub> lines, we may have discovered a massive cloud on its way to form a SSC within the next few Myr. However, this conclusion is only tentative, and will remain incomplete, until we obtain the missing information about the mass, the density structure and the kinematics of the bulk of the gas. The H<sub>2</sub> line emission provides this information only for the fraction of warm, shock-heated gas. The missing information can be obtained with ALMA.

## 6. Discussion

Our observations are related to two main questions in the field of star formation. How do super star clusters form? What are the roles of turbulence and stellar feedback in regulating the star formation efficiency in galaxy mergers? We discuss how our observations and interpretation may be of general relevance for these questions.

### 6.1. The formation of super-star clusters

Star formation is the result of the hierarchical structure of the molecular interstellar medium established by turbulent compression and gravitational contraction (Mac Low & Klessen 2004).

The available gas fragments over a range of masses and time scales. Massive clusters form at different times from the densest and most massive gas concentrations. For SGMC 2, this view is supported by the presence of two massive clusters (the near-IR SSC and the compact ionized source), which have formed before the compact H<sub>2</sub> source. More clusters, too small to be identified individually, are likely to have formed or to be in the process of being formed. Thus, the formation of super star clusters in SGMC 2 can be understood within the same framework as the formation of smaller clusters in disk galaxies like the Milky Way.

Our work highlights three physical parameters which may contribute to account for the formation of exceptionally massive clusters in the overlap region of the Antennae. These may be of general relevance for the formation of super star clusters in other extragalactic objects: other interacting/merging galaxies, and also starbursts and irregular dwarf galaxies (Keto et al. 2005; Weidner et al. 2010). (1) The presence of compressive motion on large scales which collects the gas. The formation of the SGMC 2 complex and that of the compact H<sub>2</sub> source is driven by the galaxy interaction. The large scale dynamics triggers the gas compression necessary for their formation and their subsequent growth by gas accretion. (2) As discussed in earlier studies (Escala & Larson 2008; Weidner et al. 2010), shear is the second key parameter in the formation of massive clusters because it sets the maximum mass that the gas self-gravity can collect. In the Antennae, the present geometry of the interaction, which temporarily makes the tidal forces compressive (Renaud et al. 2008), is favorable to the formation of massive clusters. As discussed by Renaud et al. (2009) such conditions occur repeatedly in galaxy mergers. (3) High turbulence is an additional key parameter. Since the Jeans mass is proportional to  $\sigma^4$  (see Sect. 5.1), a high value of the velocity dispersion  $\sigma$  scales up the masses of the clouds formed by gravitational fragmentation. To form a super star cluster, it is not sufficient to bind a large mass of gas. It is also necessary that the star formation efficiency becomes high when the gas mass is highly concentrated. It is likely that high turbulence is a key factor which prevents star formation to be efficient before the cloud mass has been concentrated by gravity. This is a prerequisite to form a dense, potentially bound, cluster rather than a loose OB association (Elmegreen 2008).

### 6.2. The impact of turbulence

The impact of turbulence on the star formation efficiency is a long standing topic of research (Mac Low & Klessen 2004). Krumholz & McKee (2005) and Padoan & Nordlund (2011) used numerical simulations to quantify the dependence of the star-formation rate per free-fall time on the Mach number of turbulence. Both agree that, independent of the mean cloud density, for a cloud near virial equilibrium, the fraction of the gas mass that is unstable to collapse is small. If this is correct, then the formation of dense clusters within a cloud supported by turbulence must occur over several cloud crossing times as argued by Tan et al. (2006) and Krumholz et al. (2006). Elmegreen (2008) expresses a different view point by proposing that star formation becomes efficient within cores with a mean density  $> 10^4 \text{ H cm}^{-3}$  independent of turbulence.

These ideas are being tested against observations of galactic star forming regions and cores, which are far more detailed than the present information we have on the compact H<sub>2</sub> source. High angular resolution observations of molecular lines at mm wavelengths, which unlike the near-IR H<sub>2</sub> lines will trace the kinematics of the bulk of the gas and the source density structure, would be needed for a detailed study of the formation of super

star clusters on the example of this source, and if it is consistent with present ideas based on observations of lower mass and less turbulent cores. Here we only make preliminary remarks that can soon be tested with ALMA. The mean density of the compact H<sub>2</sub> source is  $\sim 10^4 \text{ H cm}^{-3}$ . We estimate its formation time scale to at least  $10^6 \text{ yr}$ , but the star-formation efficiency is still very small (stellar to gas mass ratio  $\sim 0.3\%$ ). This remarkable result may indicate that the high turbulence (1D velocity dispersion  $\sim 20 \text{ km s}^{-1}$ ) has been very effective at preventing star formation. Star formation may occur rapidly once the rate of mass accretion becomes insufficient to drive the present amplitude of turbulence. The fact that stars may be forming out of gas which has lost the turbulent energy it had during the initial gravitational contraction reduces the requirement on the star formation efficiency to form a bound stellar cluster.

### 6.3. Star formation efficiency

The star formation rate (SFR) in the Antennae merger has been estimated to  $20 M_\odot \text{ yr}^{-1}$  for a total molecular gas mass  $\sim 10^{10} M_\odot$ . Local values measured from CO and H $\alpha$  images of the Antennae agree with the general correlation between the SFR and molecular gas surface densities, the Schmidt-Kennicutt law (Kennicutt 1998; Zhang et al. 2001). The burst of star formation observed in the overlap region follows mainly from the high surface density of molecular gas with only a small (a factor  $\sim 3$ ) enhancement of the star formation efficiency with respect to the Galactic value. This enhancement comes from the non-linear dependence of the SFR on the surface density of gas. The star formation rate per unit gas mass in the SINFONI field of view is similar to the global value. Based on their Spitzer and Herschel data, Brandl et al. (2009) and Klaas et al. (2010) find an SFR of  $\sim 0.7 M_\odot \text{ yr}^{-1}$  for a molecular mass of  $4 \times 10^8 M_\odot$ .

To compute the star formation efficiency, we consider that star formation is triggered by gas compression and occurs over the characteristic time,  $\sim 10 \text{ Myr}$ , over which the tidal interaction is compressive (Renaud et al. 2008). This is also the crossing time across the SINFONI field of view for the CO line width. Over this time the gas mass converted into stars is  $7 \times 10^6 M_\odot$ , which yields a star formation efficiency of 2%. The SSC accounts for a significant fraction of this stellar mass (see estimates of the cluster mass in Table 1). For the SGMC 2 complex, like for the compact H<sub>2</sub> source, the low star-formation efficiency may result from the strong, driven turbulence. For the molecular complex, the star-formation efficiency may remain low until it is disrupted by the tidal interaction. If turbulence continues to be driven by on-going accretion, it is possible that the CO complex will be dispersed without losing its turbulent energy. It will be interesting to extend the present study to other complexes in the overlap region to test this idea.

### 6.4. Stellar feedback

It is interesting to compare this analysis and interpretation of observational data with numerical simulations. In their Figure 1, Karl et al. (2011) compare the star-formation rates in recent numerical simulations of the Antennae. All simulations predict a significant enhancement of the star-formation efficiency, relative to its value in the two spirals prior to interaction, after pericenter passage. In the simulations, the enhancement in the star formation efficiency is triggered by the gas compression and subsequent gas cooling. For several runs the enhancement is one order of magnitude or more, i.e. larger than that derived from obser-

vations. Karl et al. (2011) present new simulations that quantify the impact of stellar feedback on the star formation efficiency, and argue that it is necessary to invoke stellar feedback to compensate for the gas cooling. Our H<sub>2</sub> observations do not support this idea.

In Sect. 5, we argue that the gas turbulence is driven by the galaxy interaction. Stellar feedback is energetically significant but not a key contributor to the turbulent energy of the molecular gas. This holds for the SGMC 2 complex and the compact H<sub>2</sub> source. We start discussing feedback on the scale of the SGMC 2 complex using Starburst99 models. For a Salpeter IMF and continuous star formation over 10 Myr, the mechanical energy associated with stellar winds and supernovae explosions is  $L_{\text{Mech}}(\text{SF}) \sim 4 \times 10^7 \times (\text{SFR}/0.7 M_\odot \text{ yr}^{-1}) L_\odot$ . Most of this energy is released by the stars in the SSC. The non-thermal component of the radio flux from the SSC (Neff & Ulvestad 2000) indicates that the SSC has evolved to an age where the most massive stars are exploding as supernovae. For a stellar mass of a few  $10^6 M_\odot$ , the mechanical power from stellar winds and supernovae is also a few  $10^7 L_\odot$ . This value is one order of magnitude larger than the H<sub>2</sub> luminosity of the extended emission, but the lack of enhancement of the H<sub>2</sub> line width towards the SSC is evidence that stellar feedback does not contribute significantly to driving the turbulent kinetic energy of the H<sub>2</sub> gas. The energy from stellar feedback must be mostly transferred to the hot X-ray emitting plasma (Baldi et al. 2006). We plan to test this tentative conclusion with additional SINFONI data towards other super star clusters in the overlap region.

For the compact source, we estimate the star formation rate by dividing the stellar mass of  $4 \times 10^4 M_\odot$  (from Sect. 3.3) by the formation time scale  $t_{\text{acc}} \sim 3 \times 10^6 \text{ yr}$  (from Sect. 5.3). We find  $\text{SFR} \sim 10^{-2} M_\odot \text{ yr}^{-1}$ . For this rate, the mechanical energy from stellar winds is two orders of magnitude smaller than the H<sub>2</sub> luminosity of the compact source. Using formula (6) in Matzner (2002) we verified that the contribution from proto-stellar winds around low mass stars is also much smaller than the H<sub>2</sub> luminosity.

## 7. Conclusions

We presented an analysis of VLT/SINFONI near-IR imaging spectroscopy of the region with the brightest H<sub>2</sub> rotational line emission in the Antennae overlap region, which has previously been identified with Spitzer/IRS spectroscopy. The region encompasses one of the supergiant molecular complexes, SGMC 2, discovered through CO interferometric observations. It corresponds to one of the brightest FIR knots in the overlap region, and is near a young ( $\sim 5 \text{ Myr}$ ) super star cluster previously identified in NIR imaging including HST imaging. Our imaging spectroscopy provides us with constraints on the spatial distribution, kinematics and excitation of the H<sub>2</sub> and H $\alpha$  gas out to a radius of 300 pc from this cluster. Based on these observations, we investigated how the large-scale gas dynamics may trigger the formation of the SSC and regulate the star formation efficiency. We have also discussed how the observations and our interpretation may be of general relevance for the formation of dense massive clusters and the efficiency of star formation in mergers. We list our main results.

- We find extended near-IR H<sub>2</sub> line emission across much of our SINFONI field-of-view with broad line widths (FWHM  $\sim 200 \text{ km s}^{-1}$ ), larger than those measured from CO and Br $\gamma$  at the same position (which are 70 and  $130 \text{ km s}^{-1}$ , respectively). The line width is commensurate with a large-scale

velocity gradient across the field. We argue that this extended emission component traces a convergent turbulent flow driven by the galaxies interaction. Spectral diagnostics show that the H<sub>2</sub> emission is shock powered and traces the dissipation of the gas turbulent kinetic energy.

- The data reveal a compact H<sub>2</sub> source (50 pc diameter) with a K-band spectrum showing only H<sub>2</sub> line emission. The H<sub>2</sub> lines are spectrally resolved with a width  $\sim 150 \text{ km s}^{-1}$  (FWHM). The H<sub>2</sub> emission from this source is also shock excited. The cloud virial mass is  $\sim 1 \times 10^7 M_{\odot}$ . The absence of Bry emission and of some obvious counterpart in the radio continuum set a low limit on the mass of newly formed stars (stellar mass fraction  $\sim 0.3\%$ ). To our knowledge, this is the first time that an extragalactic source with such characteristics is identified.
- The width of the H<sub>2</sub> spectra show that the SGMC 2 complex and the compact source are both associated with gas which is too turbulent to be bound. We argue that this suggests that the H<sub>2</sub> emission is powered by gas accretion. We show that the required accretion rate is of the right order of magnitude to drive the gas turbulence and to account for the formation of both the SGMC 2 complex and the compact source by accretion.
- By observing gas cooling through H<sub>2</sub> lines, we may have discovered a massive cloud on its way to form an SSC within the next few Myr. However, this conclusion is only tentative, and will remain incomplete, until we obtain the missing information about the mass, the density structure and the kinematics of the bulk of the gas. The H<sub>2</sub> line emission provides this information only for the warm shock excited fraction. The missing information can be obtained with ALMA.
- We propose that the strong turbulence observed in the extended emission and the compact H<sub>2</sub> source is of general relevance for the formation of SSCs in two ways. A high value of the gas velocity dispersion increases the masses of the clouds formed by gravitational fragmentation. It may also prevent star formation to be efficient before the cloud is fully formed, i.e. as long as turbulence is driven by accretion. Clusters may form out of gas which has lost much of the turbulent energy it had during gravitational formation of the pre-stellar cloud. If this is correct, then it reduces the requirement on the star-formation efficiency to form a bound stellar cluster.
- Our observations highlight the role of merger-driven turbulence in regulating the star-formation efficiency in interacting galaxies. Within the field of view of our SINFONI observations, about 2% of the molecular gas has been turned into stars. We relate this small efficiency to the fact that the gas turbulence does not dissipate because it continues to be driven by on-going accretion.

**Acknowledgements.** The authors wish to thank the staff at the VLT and at the CFHT for making these observations. We are grateful to C. Wilson for providing us with her OVRO CO data. We would like to thank the anonymous referee for the detailed and constructive report that helped us in the interpretation of our data. We thank B. Elmegreen, P. Guillard, P. Hennebelle and G. Pineau des Forets for helpful discussions at an early stage in the writing of this paper. C.H. acknowledges support from a CNRS-CONICYT scholarship. This research is funded by CONICYT and CNRS, in accordance with the agreement written on December 11, 2007.

## References

- Appleton, P. N., Xu, K. C., Reach, W., et al. 2006, ApJ, 639, L51
- Baldi, A., Raymond, J. C., Fabbiano, G., et al. 2006, ApJ, 636, 158
- Barnes, J. E. & Hernquist, L. 1996, ApJ, 471, 115
- Bonnet, H., Abuter, R., Baker, A., et al. 2004, The Messenger, 117, 17
- Brandl, B. R., Snijders, L., den Brok, M., et al. 2009, ApJ, 699, 1982
- Cluver, M. E., Appleton, P. N., Boulanger, F., et al. 2010, ApJ, 710, 248
- Eisenhauer, F., Abuter, R., Bickert, K., et al. 2003, in SPIE, ed. M. Iye & A. F. M. Moorwood, Vol. 4841, 1548–1561
- Elmegreen, B. G. 2007, ApJ, 668, 1064
- Elmegreen, B. G. 2008, ApJ, 672, 1006
- Escala, A. & Larson, R. B. 2008, ApJ, 685, L31
- Falgarone, E., Verstraete, L., Pineau Des Forets, G., & Hily-Blant, P. 2005, A&A, 433, 997
- Fall, S. M., Chandar, R., & Whitmore, B. C. 2005, ApJ, 631, L133
- Fall, S. M., Krumholz, M. R., & Matzner, C. D. 2010, ApJ, 710, L142
- Flower, D. R. & Pineau Des Forets, G. 2010, MNRAS, 406, 1745
- Giannini, T., McCaughan, C., Nisini, B., et al. 2006, A&A, 459, 821
- Gilbert, A. M. & Graham, J. R. 2007, ApJ, 668, 168
- Godard, B., Falgarone, E., Gerin, M., Hily-Blant, P., & de Luca, M. 2010, A&A, 520, A20+
- Guillard, P., Boulanger, F., Pineau Des Forets, G., & Appleton, P. N. 2009, A&A, 502, 515
- Haas, M., Chini, R., & Klaas, U. 2005, A&A, 433, L17
- Heitsch, F., Burkert, A., Hartmann, L. W., Slyz, A. D., & Devriendt, J. E. G. 2005, ApJ, 633, L113
- Hennebelle, P., Banerjee, R., Vázquez-Semadeni, E., Klessen, R. S., & Audit, E. 2008, A&A, 486, L43
- Ho, L. C. & Keto, E. 2007, ApJ, 658, 314
- Huff, E. M. & Stahler, S. W. 2007, ApJ, 666, 281
- Hummer, D. G. & Storey, P. J. 1987, MNRAS, 224, 801
- Jog, C. J. & Ostriker, J. P. 1988, ApJ, 328, 404
- Karl, S. J., Fall, S. M., & Naab, T. 2011, ApJ, 734, 11
- Karl, S. J., Naab, T., Johansson, P. H., et al. 2010, ApJ, 715, L88
- Kennicutt, Jr., R. C. 1998, ApJ, 498, 541
- Keto, E., Ho, L. C., & Lo, K.-Y. 2005, ApJ, 635, 1062
- Klaas, U., Nielbock, M., Haas, M., Krause, O., & Schreiber, J. 2010, A&A, 518, L44+
- Klessen, R. S. & Hennebelle, P. 2010, A&A, 520, A17+
- Kristensen, L. E. 2007, PhD thesis, LERMA, Observatoire de Paris-Meudon; LAMAP, Université de Cergy-Pontoise
- Krumholz, M. R., Matzner, C. D., & McKee, C. F. 2006, ApJ, 653, 361
- Krumholz, M. R. & McKee, C. F. 2005, ApJ, 630, 250
- Le Petit, F., Nehmé, C., Le Bourlot, J., & Roueff, E. 2006, ApJS, 164, 506
- Leitherer, C., Ortiz Otálvaro, P. A., Bresolin, F., et al. 2010, ApJS, 189, 309
- Leitherer, C., Schaerer, D., Goldader, J. D., et al. 1999, ApJS, 123, 3
- Mac Low, M.-M. & Klessen, R. S. 2004, Reviews of Modern Physics, 76, 125
- Maret, S., Bergin, E. A., Neufeld, D. A., et al. 2009, ApJ, 698, 1244
- Matzner, C. D. 2002, ApJ, 566, 302
- McKee, C. F. & Ostriker, E. C. 2007, ARA&A, 45, 565
- Mengel, S., Lehnert, M. D., Thatte, N., & Genzel, R. 2005, A&A, 443, 41
- Neff, S. G. & Ulvestad, J. S. 2000, AJ, 120, 670
- Nesvadba, N. P. H., Boulanger, F., Salomé, P., et al. 2010, A&A, 521, A65+
- Nesvadba, N. P. H., Lehnert, M. D., Davies, R. I., Verma, A., & Eisenhauer, F. 2008, A&A, 479, 67
- Nesvadba, N. P. H., Lehnert, M. D., De Breuck, C., Gilbert, A., & van Breugel, W. 2007, A&A, 475, 145
- Ogle, P., Boulanger, F., Guillard, P., et al. 2010, ApJ, 724, 1193
- Padoan, P. & Nordlund, Å. 2011, ApJ, 730, 40
- Puxley, P. J., Hawarden, T. G., & Mountain, C. M. 1990, ApJ, 364, 77
- Renaud, F., Boily, C. M., Fleck, J., Naab, T., & Theis, C. 2008, MNRAS, 391, L98
- Renaud, F., Boily, C. M., Naab, T., & Theis, C. 2009, ApJ, 706, 67
- Schweizer, F., Burns, C. R., Madore, B. F., et al. 2008, AJ, 136, 1482
- Scoville, N. Z., Sanders, D. B., & Clemens, D. P. 1986, ApJ, 310, L77
- Tan, J. C., Krumholz, M. R., & McKee, C. F. 2006, ApJ, 641, L121
- Teyssier, R., Chapon, D., & Bournaud, F. 2010, ApJ, 720, L149
- Tody, D. 1993, in Astronomical Society of the Pacific Conference Series, Vol. 52, Astronomical Data Analysis Software and Systems II, ed. R. J. Hanisch, R. J. V. Brissenden, & J. Barnes, 173–
- Vázquez-Semadeni, E., Gómez, G. C., Jappsen, A. K., et al. 2007, ApJ, 657, 870
- Vigroux, L., Mirabel, F., Altieri, B., et al. 1996, A&A, 315, L93
- Weidner, C., Bonnell, I. A., & Zinnecker, H. 2010, ApJ, 724, 1503
- Weingartner, J. C. & Draine, B. T. 2001, ApJ, 548, 296
- Whitmore, B. C., Chandar, R., Schweizer, F., et al. 2010, AJ, 140, 75
- Whitmore, B. C. & Schweizer, F. 1995, AJ, 109, 960
- Wilson, C. D., Scoville, N., Madden, S. C., & Charmandaris, V. 2000, ApJ, 542, 120
- Wilson, C. D., Scoville, N., Madden, S. C., & Charmandaris, V. 2003, ApJ, 599, 1049

- Zakamska, N. L. 2010, Nature, 465, 60  
Zhang, Q. & Fall, S. M. 1999, ApJ, 527, L81  
Zhang, Q., Fall, S. M., & Whitmore, B. C. 2001, ApJ, 561, 727